International Journal of Earth Sciences Knowledge and Applications
journal homepage: http://www.ijeska.com/index.php/ijeska
e-ISSN: 2687-5993

Research Article https://doi.org/10.5281/zenodo.22161309

Geochemical Characteristics of Dubele Lateritic Soils in the Dubele Village, Moto Greenstone Belt (Northeastern Democratic Republic of Congo): Weathering Intensity, Ferruginous Lateritization and Mafic Provenance

Innocent Agama Badriyo[1,2]*, Paulin Bamwambeye Isimbika[3], Placide Pioka La Pioka[2], Nicaise Blaise Tchuimegnie Ngongang[4], Joseph Aguma Madrakele[3]

[1]*Goma Volcano Observatory, Department of Seismology, P.O.B. 484 Goma, Democratic Republic of Congo*
[2]*Department of Geology, Faculty of Sciences and Technology, University of Goma, Goma, P.O.B. 204 Goma, Democratic Republic of Congo*
[3]*Department of Geology, Faculty of Sciences, University of Kisangani, P.O.B. 2012 Kisangani, Democratic Republic of Congo*
[4]*Department of Geology, Faculty of Sciences, University of Douala, P.O.B. 24157, Douala Cameroon*

INFORMATION

Article history
Received 04 August 2026
Accepted 22 August 2026
Published 31 August 2026

Contact
*Innocent Agama Badriyo
ibadriyo@gmail.com (IAB)
https://orcid.org/0009-0006-5065-8857

How cite
Badriyo, I.A., Isimbika, P.B., La Pioka, P.P., Ngongang, N.B.T., Madrakele, J.A., 2026. Geochemical Characteristics of Dubele Lateritic Soils in the Dubele Village, Moto Greenstone Belt (Northeastern Democratic Republic of Congo Congo): Weathering Intensity, Ferruginous Lateritization and Mafic Provenance. *International Journal of Earth Sciences Knowledge and Applications* 8 (2), 185-202.
https://doi.org/10.5281/zenodo.22161309.

Abstract
Lateritic soils developed on the Moto Greenstone Belt in the Dubele area (Watsa Territory, Haut-Uélé Province, northeastern DR Congo) were characterized geochemically to assess the weathering intensity, degree of lateritization, and parent-material affinity. Ten samples from the B horizon (~0.5 m depth) were analyzed using ED-XRF. The major element assemblage is dominated by SiO_2, Fe_2O_3, and Al_2O_3, with marked depletion of alkalis and alkaline earths, reflecting intense leaching under humid tropical conditions. High CIA (mean 96.50), PIA (mean 95.26), and MIA values confirm the near-complete breakdown of the primary feldspar and ferromagnesian assemblages. The S/R ratios (0.91–1.62) and Fe_2O_3/Al_2O_3 ratios (mean 1.92) classify the materials as ferruginous laterites at the boundary with lateritic rocks, whereas the IOL values (58.18–71.99) place them at an intermediate stage of lateritic evolution. The Al_2O_3/TiO_2 ratios (mean 8.83) and major-element discriminant functions point unambiguously to a mafic protolith, corroborated by elevated Cr, Ni, and V concentrations. Arsenic concentrations reach up to 2973 ppm, may probably originate from the supergene alteration of arsenopyrite and hydrothermal sulfide assemblages within the mineralized basement. These results provide the first geochemical dataset on lateritic soils and highlight the potential of lateritic geochemistry as an exploration tool within the auriferous Moto Greenstone Belt.

Keywords
Lateritic soils, Chemical weathering, Ferruginous laterite, Mafic provenance, High Arsenic content, Moto Greenstone Belt

1. Introduction

Lateritic weathering represents one of the most advanced geochemical processes in tropical and subtropical regions, where the intensive leaching of mobile elements is accompanied by the relative enrichment of iron, aluminum, titanium, and certain trace elements (Ghosh and Guchhait, 2019). The supergene redistribution of elements derived from primary mineralization confers dual significance on lateritic profiles for mineral exploration and environmental assessment (Iglesias-Martínez et al. 2024; Abedini and

Calagari, 2015). The Dubele area lies within the Moto Gold District (MGD), a Neoarchean terrane in northeastern DR Congo, recognized for its significant gold mineralization (Allibone et al., 2020). In tropical environments developed on ancient basement rocks, prolonged meteoric weathering generates thick profiles organized into successive saprolite, clay-rich, and ferruginous horizons, reflecting the progressive disaggregation of parent rocks, silica mobilization, relative enrichment in iron or aluminum sesquioxides, and neoformation of secondary minerals such as kaolinite, goethite, and hematite (Butt and Anand, 2025; Adeola and Dada, 2017). Ferruginization does not follow the logic of monotonous iron accumulation but responds to the local conditions of drainage, hydration, and morphological stability of the landscape (Aboubakar et al., 2026; Beauvais, 1999).African literature on lateritic soils has largely focused on their geotechnical properties (Aboubakar et al. 2026; Kaboré et al. 2026; Oyelami and Van Rooy 2016; Mvindi et al., 2024), whereas their geochemical provenance and degree of weathering have been weakly explored in several regional studies (Adama et al., 2025; Aboubakar et al., 2026; Widdowson, 2007; Freyssinet et al., 2005).

The geochemistry of lateritic soils remains unexplored in the Democratic Republic of Congo, despite the widespread distribution of laterites across the territory and their extensive use in mining and civil engineering applications. Given that the geochemical composition of lateritic soils results from the combined influence of geological setting, topography, and climate, this study addresses two central questions: (i) what is the degree of chemical weathering, and (ii) how well do the Dubele lateritic soils preserve the geochemical signature of the underlying parent rocks? We pursued four objectives: describing the major- and trace-element geochemistry of the soils; measuring weathering intensity using established geochemical indices; evaluating the extent of lateritization and classifying the soils; and determining the nature of the source rocks through provenance discrimination diagrams and trace-element patterns, compared against lateritic profiles worldwide.

2. Geological Setting

2.1. Global Geodynamic Framework

The Congo Basin is an intracratonic depression of approximately 3.7 million km2 within the stable region of the African Plate (Braun et al., 2026). Its Precambrian basement, amalgamated between the Paleoarchean and Neoproterozoic, is dominated by the Congo Craton, subdivided into three subunits: the southwestern Congo Craton (Kasai-Kwango and Chaillu-Ntem blocks), northeastern Congo Craton (Bomu-Kibalian Craton, Western Nile Complex, and Ugandan blocks), and Central Congo Craton, concealed beneath sedimentary cover (Braun et al., 2026; de Wit and Linol, 2014). This basement was successively reworked by the Eburnean Orogeny, Kibaran event (Tack et al., 2010), and Pan-African Orogeny, which locked in its definitive structural configuration (Braun et al., 2026).

The Moto Gold District (MGD) is part of the Bomu-Kibalian Craton. The 8–12 km thick intracratonic sedimentary sequence spans the Stenian-Tonian Mbuji-Mayi Supergroup, correlated with the fragmentation of Rodinia (Braun et al., 2026; Kadima et al., 2011), through the Cretaceous Congo Supergroup, with an extensive lateritic cover in the studied area representing the legacy of long-term weathering under humid tropical conditions (Guillocheau et al., 2018; Burke et Gunnell, 2008).

2.2. Regional Geology

The Bomu-Kibalian Craton, exposed in the Haut-Uélé Province of eastern DRC (Fig. 1a and b), comprises two principal units: the Bomu Complex and Kibalian Greenstone Region (Birimwiragi Namogo et al., 2025; Goodwin, 1991; Cahen et al., 1984).

The latter hosts world-class orogenic gold deposits and forms the geological backbone of the Moto Gold District (Kabete et al., 2021a). Situated within the Northern Kibalian Superterrane (Fig. 1b), the MGB consists of volcanosedimentary rocks deposited between ca. 2640 Ma and ca. 2625 Ma (Allibone et al., 2020; Turnbull et al., 2021; Mpaka et al., 2023). U-Pb geochronology has identified three successive magmatic episodes: (1) mafic-granitic syn-volcanic magmatism at ca. 2680–2640 Ma; (2) tonalitic-granodioritic magmatism at ca. 2640–2600 Ma; and (3) syenite, quartz monzonite, and felsic granite intrusions at ca. 2600–2570 Ma and emplaced along reactivated extensional zones (Kabete et al., 2021b). Tectonic uplift was dated to ca. 2603 Ma, coinciding with a hydrothermal episode at ca. 2605–2590 Ma, associated with gold mineralization, while definitive cratonization of the Superterrane occurred at ca. 2556 Ma, following the collision between the Western Ituri and Kilo Terranes (Kabete et al., 2021b). Within the Moto Gold Territory, the Kibali district hosts several major deposits, including KCD (Karagba–Chauffeur–Durba) and its satellites (Gorumbwa, Kombokolo, Rhino, and Agbarabo), Pakaka–Tete Bakangwe, and Kalimva, aligned along a ~60 km belt-parallel structure known as the Kibali–Zani Trend (Mpaka et al., 2023).

The stratigraphy of the district comprises a hanging wall of metamorphosed and altered basalts and volcanoclastics and a footwall of gritstone, sandstone, conglomerates, and banded iron formations (BIF) (Mpaka et al., 2023; Allibone et al., 2020). Approximately 90% of gold is hosted by auriferous pyrite, occurring in five paragenetic stages: an early sedimentary generation; a second enriched in V, La, Ti, and Cr recording sulfidation on Banded Iron Formation (BIF); a third, more auriferous generation representative of the principal mineralizing fluid; a fourth formed by carbonate replacement; and a fifth, paragenetically late generation (Mpaka et al., 2023; Allibone et al., 2020). At the scale of the eastern Congo Basin, low-relief landscapes are dominated by in situ iron accumulation through geochemical weathering and saprolite production (Braun et al., 2026; Bitom et al., 2004; Temgoua et al., 2002), whereas proximity to the Albertine Rift shoulder imposes a dissected topography conducive to multilevel stepped lateritic sequences (Braun et al. 2026; Guillocheau et al., 2018). The Dubele area, within the Watsa Territory of the Haut-Uélé Province (Figs. 1a–c), belongs to the Moto gold domain and is locally developed

within a greenstone belt. The Watsa Territory is predominantly underlain by Archean formations (Kabete et al., 2021a), with more than 90% of its surface occupied by mafic-felsic granite–gneiss with greenstone rafts, whereas a restricted northern zone exposes thermally and tectonically reworked Archean to Neoproterozoic rocks (Fig. 1c).

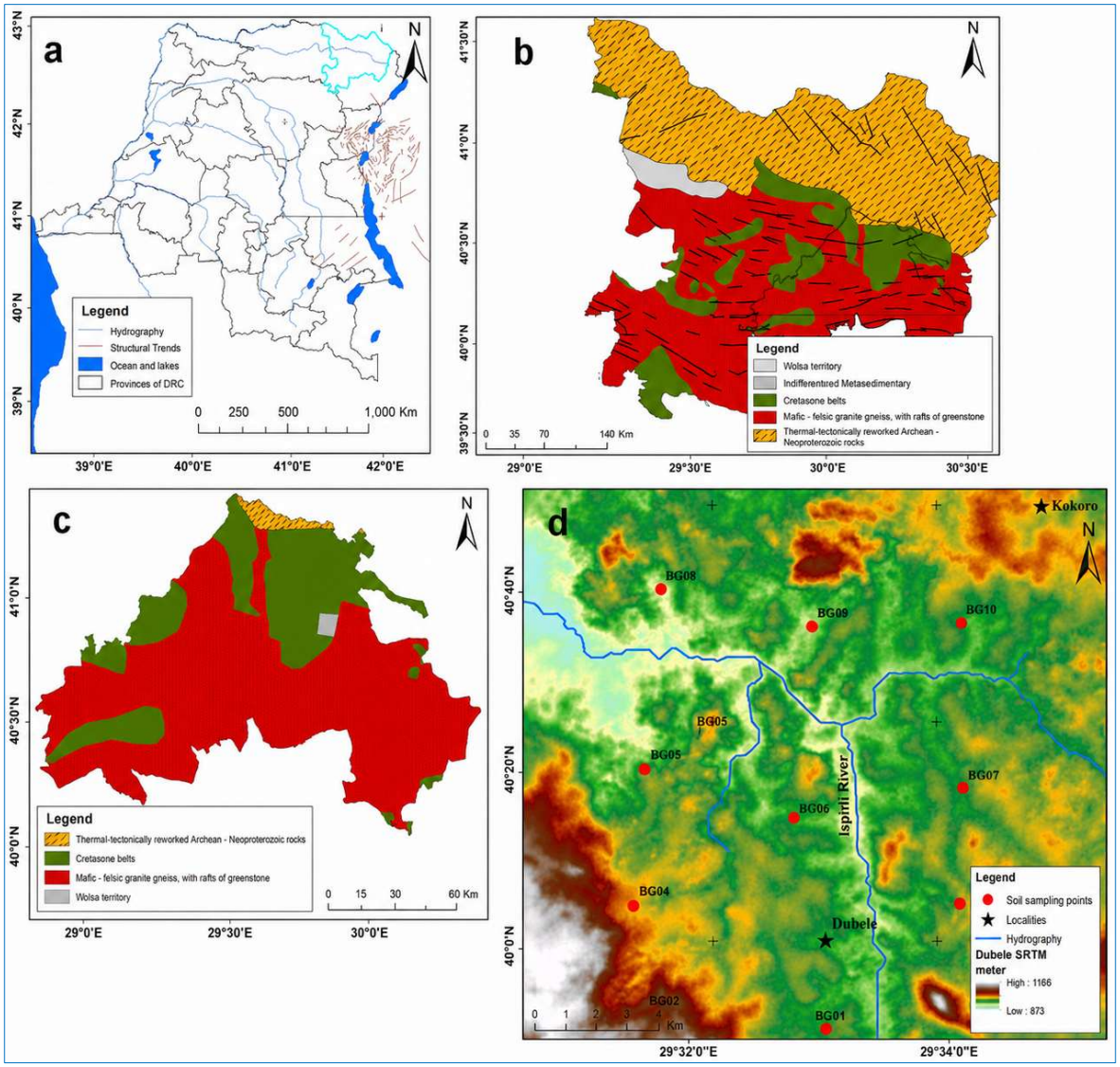

Fig. 1. (a) Map of the Democratic Republic of Congo, highlighting the Haut-Uélé Province. (b) Geological map of Haut-Uélé Province (modified from Kabete et al. (2021a)). (c) Geological map of the Watsa Territory showing the location of the study area. (d) Sample location map showing the localities, hydrography, and topography of the study area

2.3. Physical Setting of the Study Area

The Dubele area is located between latitudes 2°53′00″ N and 2°58′00″ N and longitudes 29°31′00″ E and 29°35′00″ E, at elevations ranging from 863 to 1166 m a.s.l. (Fig. 1d) within the Watsa Territory of Haut-Uélé Province in the northeastern Democratic Republic of Congo. The Watsa Territory experiences a hot and humid tropical climate characterized by alternating prolonged rainy and relatively short dry seasons (Table 1; Fig. 2). According to the Köppen–Geiger classification, the region falls within the tropical savanna climate category (Aw), approaching the transition to a tropical monsoon climate (Am) owing to its high annual rainfall (Beck et al., 2018; Peel et al., 2007).

Climatological data from Mettelsat (Democratic Republic of Congo) for the 1991–2020 reference period indicated mean monthly temperatures ranging from 23.2 °C in July to 27.5 °C in February, with an annual mean temperature of approximately 24.4 °C (Table 1; Fig. 2). The low annual thermal amplitude of 4.3 °C reflects the thermal stability of equatorial and near-equatorial tropical regions. The rainfall regime is characterized by pronounced seasonality.

The mean annual precipitation is approximately 1,946 mm, with a gradual increase beginning in March (110 mm) and a prolonged rainy season extending from April to November. The maximum monthly rainfall was recorded in October (271 mm), followed by September (235 mm), August (220 mm) and May (215 mm). The driest period spans from December to February, during which precipitation decreases sharply to a minimum of 22 mm in January, followed by 45 mm in February and 63 mm in December (Table 1; Fig. 2).

3. Materials and Methods

3.1. Soil Sampling

Ten lateritic soil samples were collected from the Dubele area (Watsa Territory, Haut-Uélé Province, Democratic Republic of Congo). All samples were systematically recovered from the reddish B horizon at an approximate depth of 0.5 m below the ground surface to minimize the potential contamination effects associated with the artisanal mining activities. The sampling locations were georeferenced in the field using a handheld GPS unit and subsequently plotted using ArcGIS 10.8 (Fig. 1d).

3.2. Geochemical Analysis by ED-XRF Spectrometry

Sample conditioning and analysis were performed at the Central Analytical Laboratory of the Commissariat Général à l'Energie/Center Régional d'Etudes Nucléaires de Kinshasa – CGEA/CREN-K (Kinshasa, Democratic Republic of Congo) under the technical supervision of the International Atomic Energy Agency. To minimize the grain-size matrix effects and mineralogical heterogeneity inherent to iron- and aluminum-rich lateritic matrices, bulk soil samples were oven-dried, pulverized, and dry-sieved to less than 63 µm using a Retsch vibratory sieving shaker.

Table 1. Mean monthly temperature and precipitation recorded in the Watsa Territory over the 1991–2020 climatological reference period (Source: Mettelsat, Democratic Republic of Congo).

Month	January	February	March	April	May	June	July	August	Sep.	Oct.	Nov.	Dec.
T° C	25.7	27.5	24.7	24.2	24	23.5	23.2	23.7	23.7	23.5	24	24.5
P(mm)	22	45	110	180	215	190	185	220	235	271	210	63

A 5.0 g aliquot of the homogenized powder was blended with 1.0 g of Fluxana organic binder in a sealed polyethylene bag, transferred into a steel die, and compressed into a flat, homogeneous pressed pellet using a Specac hydraulic press under a controlled load of 20,000 kgf. The sample weights were recorded using a high-precision analytical balance (Mettler Toledo). Multi-elemental determination was performed by energy-dispersive X-ray fluorescence spectrometry (ED-XRF) using a SPECTRO XEPOS III spectrometer (SPECTRO Analytical Instruments GmbH, Germany), equipped with a palladium anode X-ray tube and four sequential secondary targets: Molybdenum (39.76 kV, 0.88 mA), Aluminium Oxide (49.15 kV, 0.70 mA), Cobalt (35.79 kV, 1.00 mA), and HOPG Bragg Crystal (17.40 kV, 1.99 mA). This multi-excitation configuration is specifically suited for managing spectral interferences caused by the high Fe and Al content of lateritic matrices, notably the overlapping of Fe-Kα and Fe-Kβ emission lines over adjacent trace transition metal emissions. Spectral acquisition and quantification used the FP-Pellets and TQ-Pellets Fast routines based on fundamental parameter calculations combined with empirical matrix corrections (Rousseau, 2006).

Simultaneously, the loss on ignition (LOI) was determined by calcining the powder at 1000 °C for 2 h. The numerical value was manually entered into the spectrometer software to optimize the matrix calculation for the FP method. The net peak area of the potassium $K\alpha_1$ line (E = 3.313 keV), resolved under the HOPG target configuration, was normalized against the Rayleigh and Compton scatter intensities to correct for residual matrix effects and pellet density variations (He and Van Espen, 1991). Although fusion bead preparation eliminates mineralogical effects more completely, pressed pellets combined with Compton scatter normalization and fundamental parameter corrections provide adequate matrix compensation for lateritic matrices at the concentration ranges encountered in this study, consistent with published practices for iron-rich geological samples (Rousseau, 2006; He and Van Espen, 1991). External calibration was performed using the IAEA-certified reference materials SOIL-7 (Pszonicki et al., 1984), SARM 12, and OREAS lateritic ore reference standards (specifically covering transition metals and pathfinder elements) OREAS 190 – SCP Science, nickel laterite ore certified reference material – oreas 184. The instrument detection limits were calculated as LOD = 3σ/S according to the IUPAC recommendations (Long and Winefordner 1983).

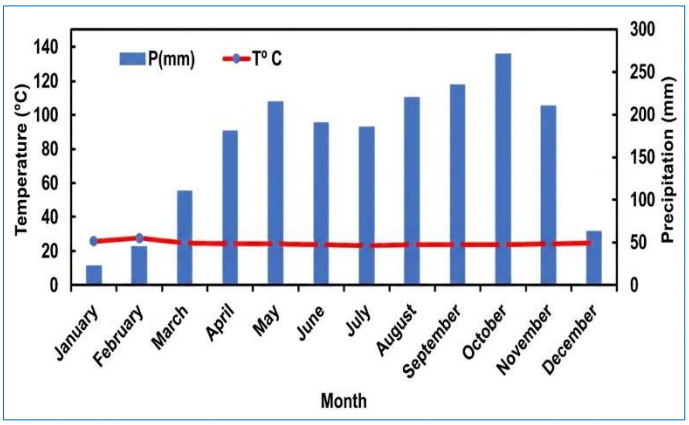

Fig. 2. Ombrothermic diagram of the Dubele area, Watsa Territory, constructed from 1991–2020 climatological normal data (Mettelsat, Democratic Republic of Congo). The diagram illustrates a long-wet season extending from March to November, with maximum rainfall in October (271 mm), and a short dry season from December to February. The mean monthly temperatures remain consistently high throughout the year, ranging from 23.2 °C to 27.5 °C

The major elements (Fe, Al, Si, Ti, and Mn) are expressed as the mass percentages of their respective oxides (wt.% Fe_2O_3, Al_2O_3, SiO_2, TiO_2, MnO,...), while trace elements (Ni, Cr, Co, Cu, Zn, As) are reported in mg kg^{-1}. All results are reported with 95% confidence intervals derived from the students' t-distribution (JCGM 100, 2008). Detection limits were typically ≤1 wt% for major oxides and lower than 0,05 % for most trace elements, in agreement with previously reported performance ranges for ED-XRF applied to geological materials.

3.3. Geochemical Data Processing

Weathering and lateritization intensity were quantified using six complementary indices calculated from molar oxide proportions, unless stated otherwise. Throughout, CaO*

denotes the fraction of calcium associated exclusively with silicate minerals, corrected for carbonate and phosphate contributions following (McLennan, 1993): CaO* = CaO - 10/3 P2O5, the unit for CaO* is molar. When CaO ≤ Na_2O, the measured value is retained; otherwise, CaO* is set equal to Na_2O.

3.3.1. S/R Ratio

The degree of lateritization was evaluated using the silica-sesquioxide ratio (S/R), defined as the weight ratio of SiO_2 to the sum of iron and aluminum sesquioxides (Fe_2O_3 + Al_2O_3). This parameter provides a straightforward measure of the relative enrichment of sesquioxides during weathering and has been widely applied to characterize the intensity of lateritic evolution in tropical soils and weathering profiles (Rossiter, 2004). Lower S/R values reflect stronger lateritization, resulting from progressive silica depletion and residual accumulation of iron and aluminum oxides. Following (Rossiter, 2004), materials with S/R < 1.33 are classified as true laterites, values between 1.33 and 2.00 correspond to lateritic materials, and values exceeding 2.00 correspond to weakly lateritized or non-lateritic materials.

3.3.2. Chemical Index of Alteration

The intensity of chemical weathering was quantified using the Chemical Index of Alteration (CIA) of, calculated as follows (Nesbitt and Young, 1982):

$$CIA = 100x[Al_2O_3/(Al_2O_3+CaO^*+Na_2O+K_2O)] \text{ (molar composition)} \quad (1)$$

The CIA tracks the progressive decomposition of feldspars and the removal of mobile cations (Ca2+, Na+, and K+) relative to the comparatively immobile Al component. Fresh igneous and metamorphic rocks yield values near 50; potassium feldspar-rich lithologies plot at 50–55; clay-rich sedimentary rocks reach 70–75; and highly weathered profiles dominated by residual kaolinite approach 100, with values above 80 conventionally read as evidence of intense chemical weathering (Nesbitt and Young, 1982; McLennan et al., 2003).

3.3.3. Plagioclase Index of Alteration

Following Fedo et al. (1997), the PIA isolates the selective alteration of plagioclase through the loss of Ca2+ and Na+ relative to alumina retained in neoformed clays as follows:

$$PIA = [Al_2O_3\text{-}K_2O/(Al_2O_3+CaO^*+Na_2O)]\times 100 \text{ (molar composition)} \quad (2)$$

Fresh plagioclase yields values near 50, whereas a fully altered end-member approaches 100. Used alongside the CIA, the PIA constrains the feldspar contribution to the overall weathering signature.

3.3.4. Mafic Index of Alteration

Babechuk et al. (2014) developed the MIA to complement the CIA by explicitly incorporating Mg and Fe behavior, capturing the alteration of ferromagnesian minerals (olivine, pyroxene, and amphibole) that dominate mafic and ultramafic rocks. Because iron's mobility during weathering depends strongly on the redox state, Fe^{3+} is largely immobilized as secondary oxyhydroxides under oxidizing conditions (Driese, 2004), while Fe^{2+} may remain mobile under reducing conditions, two end-member formulations are used:

$$MIA(O) = 100x[(Al_2O_3+Fe_2O_{3T})/(Al_2O_3+Fe_2O_{3T}+MgO+CaO^*+Na_2O+K_2O)] \quad (3)$$

Under reducing conditions, total iron is treated as mobile, alongside Mg, Ca, Na, and K:

$$MIA(R) = 100x[(Al_2O_3)/(Al_2O_3+Fe_2O_{3T}+MgO+CaO^*+Na_2O+K_2O)] \quad (4)$$

3.3.5. Weathering Index of Parker

The WIP (Parker, 1970) relies exclusively on Ca, Na, K, and Mg, making it particularly sensitive during the early weathering stages when these elements are actively mobilized. Fresh rocks exceed 100; advanced weathering drives values toward zero as mobile cations are depleted, with near-complete depletion at mature lateritic or bauxitic stages, reducing the discriminating power of the index (Babechuk et al., 2014; Price and Velbel, 2003). Following Parker (1970), the WIP was calculated as:

$$WIP = 100x[2Na_2O/0.35+MgO/0.90+2K_2O/0.25+CaO/0.70] \quad (5)$$

The weighting factors reflect the relative bond strengths of each cation within the silicate structures (Parker, 1970).

3.3.6. Index of Lateritization

Following (Babechuk et al., 2014), the IOL captures the evolving proportions of SiO_2, Al_2O_3, and Fe_2O^3 during lateritization, complementing the CIA and MIA:

$$IOL = 100\,x[(Al_2O_3+Fe_2O_3)/SiO_2+Al_2O_3+Fe_2O_3)] \quad (6)$$

The oxide concentrations are expressed as weight percentages. The IOL complements the SiO_2–Al_2O_3–Fe_2O3 ternary diagram with a scalar measure of sesquioxide enrichment during lateritic evolution (Babechuk et al., 2014).

3.3.7. Pearson Correlation Analysis

Relationships among major oxides and trace elements were evaluated using Pearson's correlation coefficient (r) in Microsoft Excel to identify linear geochemical associations among the analyzed variables. The analysis was performed on the ten Dubele soil samples (n = 10). The statistical significance of each correlation coefficient was assessed using a two-tailed Student's t-test with 8 degrees of freedom (df = n − 2 = 8). A probability level of $p < 0.05$ was considered statistically significant, with significance levels reported as $p < 0.05$, $p < 0.01$, and $p < 0.001$. Given the limited sample size, correlation coefficients were interpreted cautiously, and weak or statistically non-significant relationships were not considered robust evidence of geochemical association or common mineral hosts. The Pearson correlation coefficients and their corresponding significance levels are presented in Table 4.

3.3.8. Loss on Ignition

LOI provides a supplementary proxy for weathering intensity by tracking the abundance of hydrous secondary phases (smectite, illite, kaolinite, and iron oxyhydroxides) that

replace primary minerals as weathering advances (Hampl et al., 2023; Duzgoren-Aydin et al., 2002). Its interpretation requires caution, as the measured values depend on the specific mineralogy of the secondary assemblage present (Mvindi, 2019); considered alongside the indices above, it constrains the degree of mineral transformation across the profile (Babechuk et al., 2014).

4. Results

4.1. Field Observations

The Dubele Area constitutes an active artisanal mining zone where extraction activities target weathered horizons, particularly lateritic soils, quartz veins and alluvial deposits. Representative lateritic outcrops sampled across this area are shown in Fig. 3.

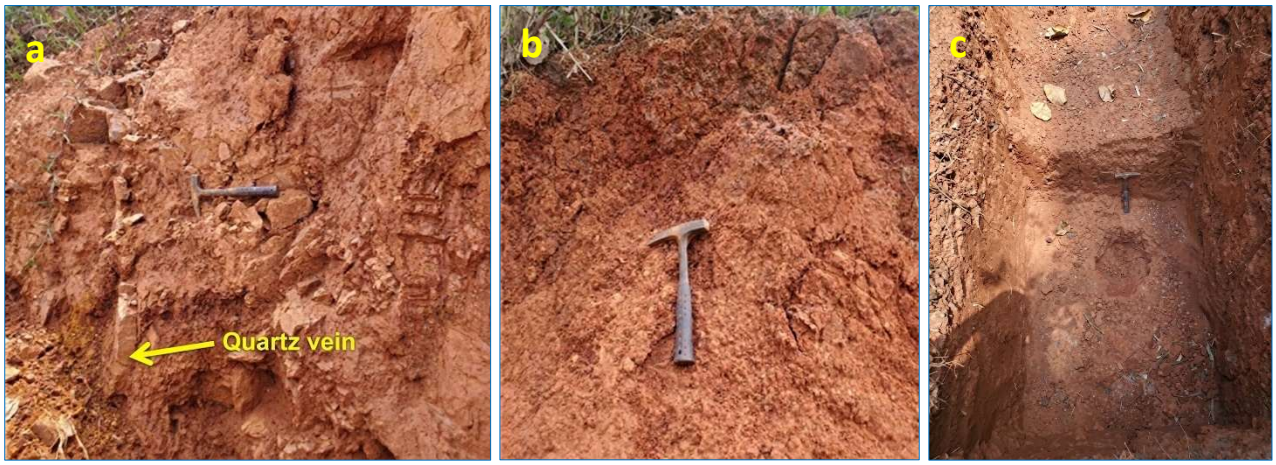

Fig. 3. Representative lateritic outcrops from the Dubele area: a) Reddish B horizon crosscut by a subvertical quartz vein exposed during terrace excavation, b) Slope of an abandoned artisanal mining terrace dominated by ferruginous material and c) Artisanal mining shaft exposing a thick, homogeneous weathered profile under active excavation

Table 2: Major and traces elements of Dubele soils

Element	BG01	BG02	BG03	BG04	BG05	BG06	BG07	BG08	BG09	BG10
SiO_2	24.56	30.50	19.00	19.29	20.30	20.65	19.24	18.96	33.35	32.28
TiO_2	1.28	3.05	1.83	2.03	1.77	2.04	1.93	0.93	1.78	1.81
Al_2O_3	16.62	19.84	10.40	12.53	17.64	14.86	7.53	8.51	24.08	23.79
Fe_2O_3	17.58	29.72	38.43	36.78	31.48	18.34	21.66	17.87	24.31	24.14
MnO	0.10	0.22	0.23	0.15	0.14	0.10	0.51	0.15	0.16	0.14
MgO	0.24	4.08	0.58	0.69	0.28	0.68	0.43	2.38	0.35	0.42
CaO	0.00	0.00	0.00	0.08	0.09	0.00	1.10	0.10	0.00	0.00
Na_2O	0.22	0.37	0.00	0.52	0.37	0.51	0.50	1.30	0.25	0.50
K_2O	0.22	0.48	0.13	0.20	0.16	0.22	0.69	0.14	0.27	0.27
P_2O_5	0.12	0.44	0.20	0.26	0.23	0.17	0.27	0.15	0.23	0.23
SO_3	0.0732	0.0421	0.0354	0.0853	0.0508	0.048	0.0978	0.0627	0.0293	0.0299
LOI	38.78	10.35	28.81	27.16	27.25	42.20	45.85	49.25	14.88	16.00
V	369.00	1032.00	555.00	1023.00	481.00	398.00	535.00	350.50	863.00	880.00
Cr	306.50	1032.00	570.50	1021.00	349.60	160.80	102.70	315.70	167.60	169.50
Co	26.00	0.00	0.00	0.00	25.20	27.00	109.00	4.90	189.00	116.00
Ni	128.40	280.70	134.00	148.90	134.60	129.20	131.30	88.60	211.80	210.20
Cu	103.60	353.50	93.40	105.50	106.10	76.90	109.20	61.20	218.90	218.60
Zn	76.90	191.70	72.10	119.80	74.70	68.20	118.00	46.50	136.40	136.70
As	306.90	2973.00	306.40	239.70	175.30	58.20	24.90	212.70	733.90	728.00
DF1	11.58	13.62	22.16	21.90	22.03	9.23	7.98	4.99	20.11	19.79
DF2	-9.79	-16.34	-15.77	-14.55	-12.68	-9.83	-11.14	-11.26	-10.88	-10.55

The exposed materials were predominantly reddish to reddish-brown, reflecting the ferrallitic weathering overprint developed above the bedrock surface. The outcrop shown in Fig. 3a exposes a reddish B horizon crosscut by a subvertical quartz vein that was revealed during the excavation of an artisanal mining terrace. The vein remains distinctly traceable within the weathered mass. Fig. 3b shows the slope of an abandoned mining terrace, composed predominantly of ferruginous material, exhibiting the same characteristic coloration. Fig. 3c reveals a relatively thick weathered profile exposed within an artisanal shaft, marked by a fairly homogeneous red color throughout its visible extent. Across all sampled sites, the materials displayed a friable texture and contained variable proportions of quartz fragments dispersed within a fine-grained, ferruginous matrix. All samples analyzed in this study were systematically collected from the B horizon at approximately 0.5 m below ground surface

4.2. Major and Trace Element Geochemistry

The major and trace element compositions of the studied lateritic soils are presented in Table 2. The major element assemblage was dominated by SiO_2, Fe_2O_3, and Al_2O_3, whereas TiO_2, MnO, MgO, CaO, Na_2O, K_2O, P_2O_5, and SO_3 occurred at subordinate concentrations.

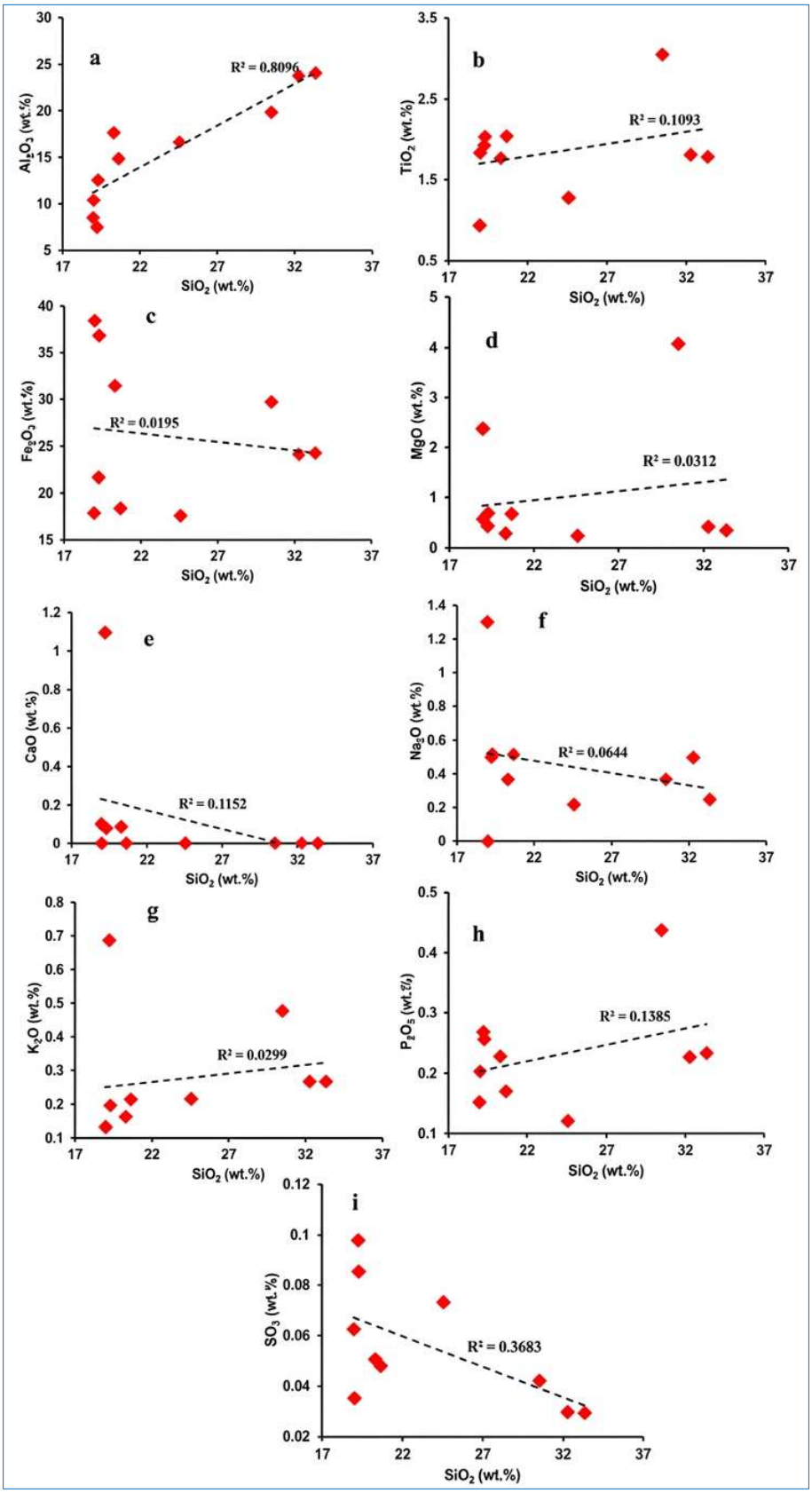

Fig. 4. Binary scatter plots of SiO_2 versus major oxides in the Dubele lateritic soils: (a) Al_2O_3, (b) TiO_2, (c) Fe_2O_3, (d) MgO, (e) CaO, (f) Na_2O, (g) K_2O, (h) P_2O_5 and (i) SO_3

The SiO_2 content ranged from 18.96 to 33.35 wt. % (mean 23.81), Al_2O_3 from 7.53 to 24.08 wt.% (mean 15.58), and Fe_2O_3 from 17.58 to 38.43 wt.% (mean 26.03), peaking in BG03 and reaching its minimum in BG01. TiO_2 content varied between 0.93 and 3.05 wt. % (mean 1.85). The remaining major oxides were consistently low: MnO (0.10–

0.51 wt.%), MgO (0.24–4.08 wt.%), CaO (0.00–1.10 wt.%), Na2O (0.22–1.30 wt.%), K2O (0.13–0.69 wt.%), P_2O_5 (0.12–0.44 wt.%), and SO_3 (0.03–0.10 wt.%). The LOI ranged from 10.35 to 49.25 wt. % (mean 30.05), highest in BG08 and lowest in BG02. Among trace elements, V (350.5–1032 ppm) and Cr (102.7–1032 ppm) show the widest spread alongside Co (4.90–189 ppm), Ni (88.6–280.7 ppm), Cu (61.2–353.5 ppm), and Zn (46.5–191.7 ppm). Arsenic exhibited the widest range of all the analyzed elements, from 24.9 to 2973 ppm (mean 575.90), with the maximum in BG02 and elevated secondary peaks in BG09 (733.9 ppm) and BG10 (728.0 ppm).

4.3. Relationships between SiO_2 and Major Elements

The binary relationships between SiO2 and the major oxides are shown in Fig. 4. Al_2O_3 showed the strongest covariation with SiO_2 (R^2 = 0.81; Fig. 4a). All other oxides showed markedly weaker relationships (R^2 < 0.15), with weak positive trends for TiO_2 (R^2 = 0.11), P2O5 (R^2 = 0.14), MgO (R^2 = 0.03), and K_2O (R^2 = 0.03), and weak negative trends for Fe2O3 (R^2 = 0.02), CaO (R^2 = 0.12), and Na_2O (R^2 = 0.06).

4.4. Weathering and lateritization Indices

The calculated indices are listed in Table 3. The CIA ranged from 82.83 to 98.79 (mean 96.50), PIA from 80.64 to 100.00 (mean 95.26), and IOL from 58.18 to 71.99 (mean 63.38). The S/R ratio ranged from 0.91 to 1.62 (mean 1.29), and the Fe2O3/Al2O3 ratio ranged from 1.01 to 3.70 (mean 1.92), reaching its maximum in BG03. The Al_2O_3/TiO_2 ratio ranged from 3.91 to 13.51 (mean 8.83), being the lowest in BG07 and the highest in BG09 and BG10. The WIP ranged from 2.70 to 19.98 (mean 9.66). MIA(O) ranged from 70.90 to 96.80 (mean 90.33) and MIA(R) from 28.65 to 58.85 (mean 43.28), with both extremes recorded in BG09 and BG03/BG08, respectively.

Table 3: Index values and chemical parameters in laterites in the study area

Sample	CIA	PIA	IOL	S/R ratio	Fe_2O_3/Al_2O_3	SiO_2/Fe_2O_3	WIP	MIA(O)	MIA(R)	Al_2O_3/TiO_2
BG01	98.59	98.71	58.20	1.50	1.06	1.40	4.53	96.32	57.49	13.01
BG02	97.45	99.58	61.90	1.33	1.50	1.03	18.69	78.06	39.89	6.50
BG03	98.60	100.00	71.99	0.92	3.70	0.49	2.70	96.27	28.65	5.67
BG04	97.22	95.52	71.88	0.91	2.94	0.52	8.55	93.40	32.49	6.17
BG05	98.12	97.92	70.76	0.91	1.78	0.64	5.78	96.77	45.22	9.98
BG06	98.44	95.81	61.65	1.32	1.23	1.13	8.44	91.08	50.93	7.29
BG07	82.83	87.22	60.27	1.53	2.88	0.89	14.38	88.34	31.14	3.91
BG08	96.23	80.64	58.18	1.62	2.10	1.06	19.98	70.90	30.28	9.12
BG09	98.79	99.46	59.20	1.43	1.01	1.37	5.54	96.80	58.85	13.51
BG10	98.78	97.73	59.76	1.40	1.01	1.34	8.02	95.39	57.88	13.14
Max	98.79	100.00	71.99	1.62	3.70	1.40	19.98	96.80	58.85	13.51
Min	82.83	80.64	58.18	0.91	1.01	0.49	2.70	70.90	28.65	3.91
Average	96.50	95.26	63.38	1.29	1.92	0.99	9.66	90.33	43.28	8.83

CIA = 100 × [Al_2O_3/(Al_2O_3+CaO+Na_2O+K_2O)] (molar composition), (Nesbitt et Young 1982); PIA = 100x [(Al_2O_3-K_2O)/(Al_2O_3+CaO*+Na_2O-K_2O)] (molar composition),(Nesbitt et Young 1982); IOL = 100 × [Al_2O_3+Fe_2O_3(T)/(SiO_2+Al_2O_3+ Fe_2O_{3T})], (Babechuk et al. 2014); WIP = 100× [2Na_2O/0.35 +MgO/0.90 + 2K_2O/0.25 +CaO/0.70], (Parker 1970); MIA = 100 × [Al_2O_3 + Fe_2O_{3T}/(Al_2O_3 + Fe_2O_{3T}+MgO+CaO*+Na_2O+K_2O)] (molar composition), (Babechuk et al. 2014). MIA(R) = 100x[(Al_2O_3)/(Al_2O_3+Fe_2O_{3T}+MgO+CaO*+Na_2O+K_2O) (molar composition) (Babechuk et al. 2014).*

5. Discussion

5.1. Significance of Field Observations

The reddish to reddish-brown coloration observed throughout the sampled outcrops (Fig. 3) is characteristic of ferruginous tropical weathering mantles and is consistent with the abundance of iron-bearing secondary minerals produced during prolonged chemical weathering (Sivarajasingham et al., 1962). Such colorations are commonly attributed to hematite and goethite, inferred to have developed through the oxidation and hydrolysis of Fe-bearing primary minerals under well-drained tropical conditions (Schwertmann, 1993; Nahon, 1991; Schwertmann and Taylor, 1989; Tardy, 1997).

The preservation of the quartz vein within the weathered horizon (Fig. 3a) underscores the contrasting geochemical behaviors of minerals during weathering: quartz ranks among the most resistant phases to chemical alteration and commonly persists within deeply weathered profiles long after the destruction of less stable silicates (Nahon 1991; Tardy 1997). In the Moto Greenstone Belt, quartz veins are frequently associated with hydrothermal mineralization systems and auriferous structures (Mpaka et al., 2023; Allibone et al., 2020) and their occurrence within the lateritic mantle indicates that weathering developed directly over mineralized bedrock under a tropical climatic regime (Fig. 2). The thickness of the weathered materials exposed in the abandoned terrace (Fig. 3b) and artisanal shaft (Fig. 3c) is consistent with extensive supergene alteration and the development of a deep, lateritic profile. In this study, no X-ray diffraction data are available for the Dubele soils, and all mineral attributions below kaolinite, goethite and hematite, are inferred from bulk-rock geochemistry and mass-balance indices rather than confirmed by direct phase identification.

5.2. Classification of Dubele laterites

Major oxide ratios provide a reliable basis for the geochemical classification of lateritic deposits (Rossiter, 2004; Aleva, 1994; Schellmann, 1986) (Fig. 5). Ferruginous laterites are characterized by Fe_2O_3/Al_2O_3 ratios greater than 1 and SiO_2/Fe_2O_3 ratios below 1.33, whereas aluminous laterites exhibit the inverse pattern. The Dubele ratios place the studied materials firmly within the ferruginous field, a classification corroborated by the Al_2O_3–SiO_2–Fe_2O_3 ternary diagram of (Aleva, 1994), on which the samples plot across a range extending from the laterite to the ferritic laterite fields (Fig. 5a). Their distribution along the S/R classification line (Fig. 5b) indicates that the Dubele materials span both true

laterites and lateritic rocks, following the thresholds of Rossiter (2004).

3.3. Major Oxide Covariations and Chemical Weathering Signatures

The strong SiO_2–Al_2O_3 covariation (R^2 = 0.81; Fig. 4a) may indicate that silica and alumina remained closely associated throughout the evolution of the Dubele lateritic soils. This behavior is characteristic of tropical weathering profiles, where feldspar and ferromagnesian silicate alterations may promote the formation of secondary aluminosilicate minerals, particularly kaolinite (Babechuk et al., 2014; Nesbitt and Young, 1982). The relatively high Al_2O_3 content of the Dubele soils (7.53–24.08 wt. %) and their elevated CIA values further support this interpretation. The relatively high Fe_2O_3 (17.58 to 38.43 wt.%) may reflect the accumulation of secondary Fe-(oxyhydr) oxide phases, potentially including goethite and hematite (Nesbitt et Young, 1982).

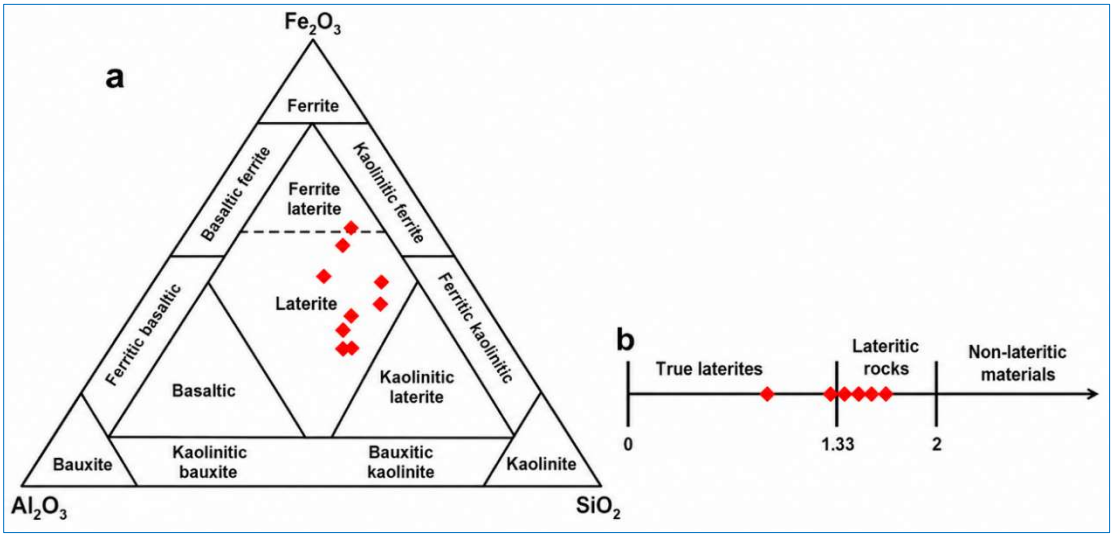

Fig. 5. Geochemical classification diagrams for Dubele lateritic soils: a) Position of the studied samples on the Fe_2O_3–Al_2O_3–SiO_2 ternary diagram (after Aleva 1994), plotted within the laterite to ferritic laterite fields and b) Distribution of the Dubele samples on the S/R classification diagram

In contrast, the decoupling of SiO_2 and Fe_2O_3 (R^2 = 0.02) may reflect independent behavior during ferruginization: silica is progressively leached from the system under humid tropical conditions, whereas iron is retained and concentrated through the inferred formation of secondary oxyhydroxides, such as goethite and hematite (Butt et Anand 2025; Okrusch and Frimmel, 2020; Freyssinet et al., 2005; Nahon, 1991; Tardy, 1997). This pattern is widely documented in ferruginous laterites from tropical settings, where Fe enrichment results primarily from residual accumulation rather than direct association with silica-bearing phases.

The weak SiO_2 correlations with MgO, CaO, Na_2O, and K_2O (Fig. 4d–g) reflect the high mobility of these cations, which are hosted primarily in feldspars, pyroxenes, and amphiboles, and are released during the earliest stages of chemical weathering (White and Brantley 2003; Nesbitt and Young 1982). Their low concentrations in the Dubele soils, combined with these weak relationships, are consistent with the elevated CIA, PIA, and MIA values. The weak SiO_2–TiO_2 correlation (R^2 = 0.11) reflects the well-established immobility of Ti, which is commonly retained in resistant accessory minerals such as rutile, anatase, ilmenite, and titanomagnetite(Babechuk et al., 2014; Hannigan and Brookfield, 2013), and is residually enriched as mobile elements are removed. The weak SiO_2–P_2O_5 correlation (R^2 = 0.14) suggests that phosphorus, typically hosted in apatite, was governed by minor accessory phases and secondary redistribution into Fe oxyhydroxides and clay minerals rather than by the silicate fraction.

Taken together, these relationships show that silica and alumina remained coupled through secondary aluminosilicate formation, whereas iron evolved independently via ferruginous mineral development. The marked depletion of alkalis and alkaline earths records extensive leaching, and the residual enrichment of titanium attests to the progressive concentration of immobile components. Under the climatic and geomorphic conditions (Figs.1d and 2), these processes collectively drove primary silicate hydrolysis and residual Fe–Al–Ti enrichment, producing the thick lateritic profile observed at the Dubele site.

5.4. Provenance of the Dubele Lateritic Soils

We used provenance discrimination diagrams based on Al_2O_3/TiO_2 ratios (Hayashi et al., 1997) and major element discriminant functions (Roser and Korsch, 1988; Hayashi et al., 1997). In the Al_2O_3–TiO_2 diagram (Fig. 6a), all samples plot within the mafic rock field (< 21; Hayashi et al., 1997).

Because both Al and Ti are relatively immobile during weathering, their ratio is widely regarded as a robust proxy for source rock composition, largely unaffected by supergene alteration (Babechuk et al., 2014; Hayashi et al., 1997), indicating that the geochemical fingerprint of the parent material was substantially preserved despite intense tropical weathering. This interpretation is corroborated by the discriminant function diagram (Fig. 6b), where all samples plot exclusively within the mafic provenance field, with no overlap in the felsic, intermediate, or sedimentary domains.

Such consistency points to derivation from ferromagnesian-rich lithologies, in agreement with the regional framework of the MGB (Kibalian), dominated by Archean volcanosedimentary sequences containing abundant mafic volcanic rocks, metabasalts, amphibolites, and related greenstone assemblages (Mpaka et al., 2023; Allibone et al., 2020), the most plausible parent materials for the lateritic cover at Dubele. The elevated Cr, Ni, and V concentrations lend further support: these elements are typically hosted by ferromagnesian minerals and Fe–Ti oxides in mafic rocks and remain relatively enriched during tropical weathering owing to their limited mobility under supergene conditions (Nahon, 1991; Tardy, 1997). The convergence of the Al_2O_3/TiO_2 ratios, discriminant function approach, and trace element budget indicates that the Dubele lateritic soils inherited a significant portion of their geochemical signature from mafic precursor rocks, a signature that was modified but not erased by intense weathering.

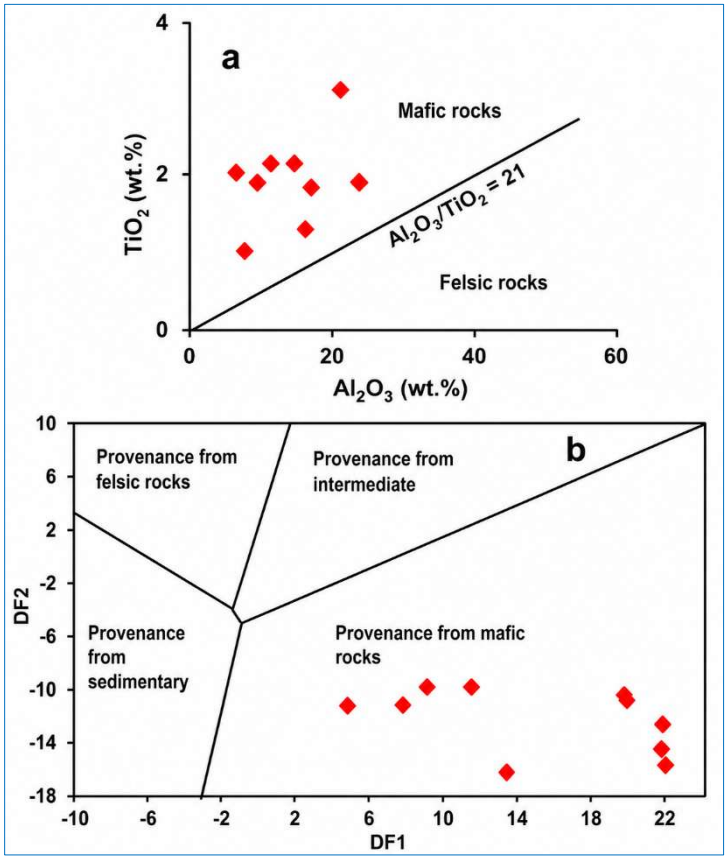

Fig. 6. Provenance discrimination diagrams for the Dubele lateritic soils: a) TiO_2 versus Al_2O_3 diagram (after Hayashi et al., 1997), with all samples plotted within the mafic protolith field and b) Major element discriminant function diagram (after Roser and Korsch, 1988), confirming a mafic source affinity. DF1 = (−1.773 × TiO_2%) + (0.607 × Al_2O_3%) + (0.76 × Fe_2O_{3T}%) + (−1.5 × MgO%) + (0.616 × CaO%) + (0.509 × Na_2O%) + (−1.22 × K_2O%) + (−9.09). DF2 = (0.445 × TiO_2%) + (0.07 × Al_2O_3%) + (−0.25 × Fe_2O_{3T}%) + (−1.142 × MgO%) + (0.432 × Na_2O%) + (1.426 × K_2O%) + (−6.861)

5.5. Weathering Evolution and Lateritization

The weathering evolution and degree of lateritization of the Dubele soils were assessed using complementary geochemical indices and ternary diagrams (Figs. 7–11) and compared with reference profiles from contrasting tropical settings: the basaltic sequences of Chhindwara (India) and mature Bidar laterites (India) (Babechuk et al., 2014), Ngaoundal laterites (Adamawa, Cameroon) (Aboubakar et al., 2026), gneiss-derived Obala laterites, central Cameroon (Mvindi, 2019), and gravel laterites (Nzabakurikiza et al., 2012). In the LOI–IOL and LOI–CIA diagrams (Fig. 7a–b), the Dubele samples plot within the transition zone between the kaolinitization and ferrugination fields (IOL: 58.18–71.99; LOI: 10.35–49.25 wt.%; CIA: 82.83–98.79), compatible with the concurrent neoformation of kaolinite-type phases and iron oxyhydroxides

Relative to Chhindwara (Babechuk et al., 2014), which remains confined to the kaolinitization field, the Dubele samples are considerably more evolved than the Chhindwara samples. Relative to Bidar (Babechuk et al., 2014), which occupies the upper ferrugination field, Dubele shows comparable CIA but a lower degree of ferruginization, reflecting the distinct behavior of the two proxies (Fig.7a). The closest regional analog is Ngaoundal, although Dubele shows a slightly higher LOI for a comparable IOL, consistent with a somewhat larger retained fraction of hydrated secondary aluminosilicates. Taken together, these relationships place the Dubele soils as strongly weathered ferruginous laterites at an intermediate stage of lateritic evolution beyond Chhindwara, close to Ngaoundal, short of the mature Bidar profiles (Fig. 7). The WIP (2.70–19.98, mean 9.66), far below the fresh-rock threshold, and the elevated PIA (80.64–100) and MIA(O) (70.90–96.80) against the markedly lower MIA(R) (28.65–58.85) confirm intense feldspar and ferromagnesian breakdown. Iron behaves as an

immobile, residually accumulated component, which is the expected signature of oxidizing tropical weathering, although the specific host phases remain to be confirmed mineralogically.

The A–L–F diagram (Fig. 8) tests this independently: the pronounced depletion of labile elements confirms a weak-to-moderate degree of lateritization, with the Dubele samples shifted well toward the Fe-rich side relative to the early-stage Chhindwara trend (Babechuk et al., 2014), while remaining short of the more advanced Bidar pathway (Babechuk et al., 2014). The Gaoundal and southern Cameroun trend (Aboubakar et al., 2025; Onana et al., 2017) seems to be close to A-F side than Dubele samples. The eastern and central Cameroun laterites (Mvindi, 2019; Nzabakurikiza et al., 2012) seem to be near the Dubele samples (Fig. 8).

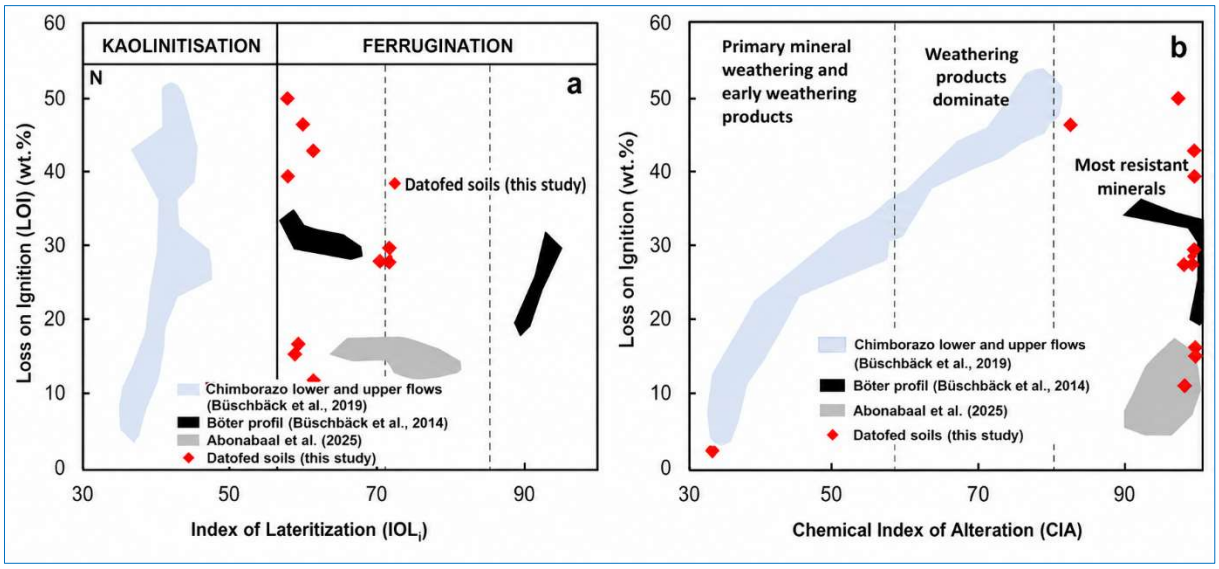

Fig. 7. Covariation diagrams for the Dubele lateritic soils (after Babechuk et al., 2014): a) Loss on ignition (LOI) versus Index of Lateritization (IOL) and b) Loss on ignition (LOI) versus Chemical Index of Alteration (CIA)

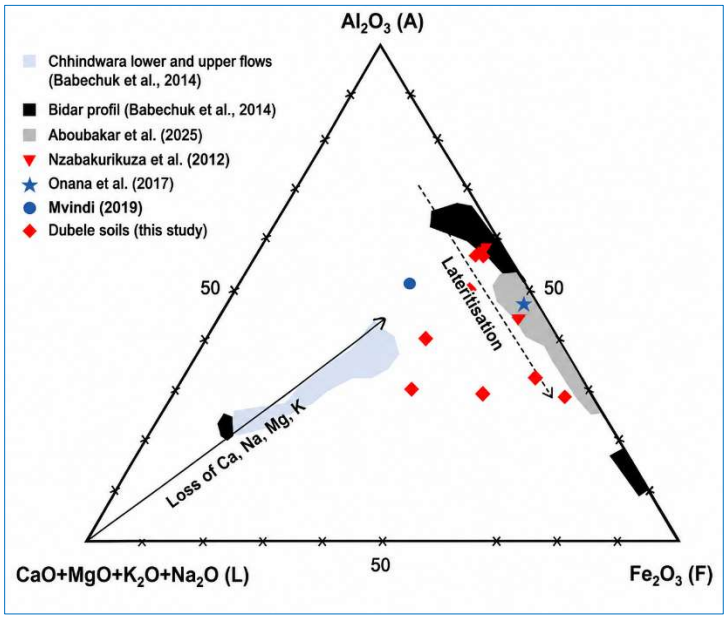

Fig. 8. Position of the Dubele lateritic soils in the A–L–F molar diagram (after Babechuk et al., 2014)

The SAF diagram (Fig. 9) offers an integrated check on this interpretation. Most of the Dubele samples plot within the moderately lateritized field, with a few extending into the weakly lateritized domain and none reaching the strongly lateritized field. This is consistent with the high CIA, moderate IOL, and elevated LOI established above, and with concurrent kaolinite formation and ferruginization rather than the wholesale replacement of aluminosilicates by iron oxides. The regional comparison again places Dubele with Ngaoundal, shows Bidar shifted toward the Fe_2O_3 apex and the strongly lateritized field, and Chhindwara toward the kaolinitized domain. Within the broader dataset of Karnataka, India (Budihal and Pujar, 2018), spanning weakly to strongly lateritized material, Dubele sits firmly in

the intermediate portion of that spectrum. The A–CN–K molar diagram (Fig. 10; Nesbitt et Young 1982) isolates the behavior of alkali and alkaline earth elements and is comparatively independent of assumptions about Fe-bearing phases. Most samples trend toward the Al apex, tracking Ca–Na depletion from plagioclase weathering, consistent with the high CIA values discussed previously. A subset was displaced slightly toward the K apex, suggesting minor, localized potassium fixation, given the uniformly low K_2O content (0.13–0.69 wt. %), this deviation does not alter the overall trajectory. The Dubele trend overlaps with those of Chhindwara (Babechuk et al., 2014) and Ngaoundal, (Aboubakar et al., 2026) whereas the Obala laterites (Mvindi, 2019) show a markedly stronger shift toward K, consistent with greater potassium retention tied to parent-rock mineralogy and secondary clay stability.

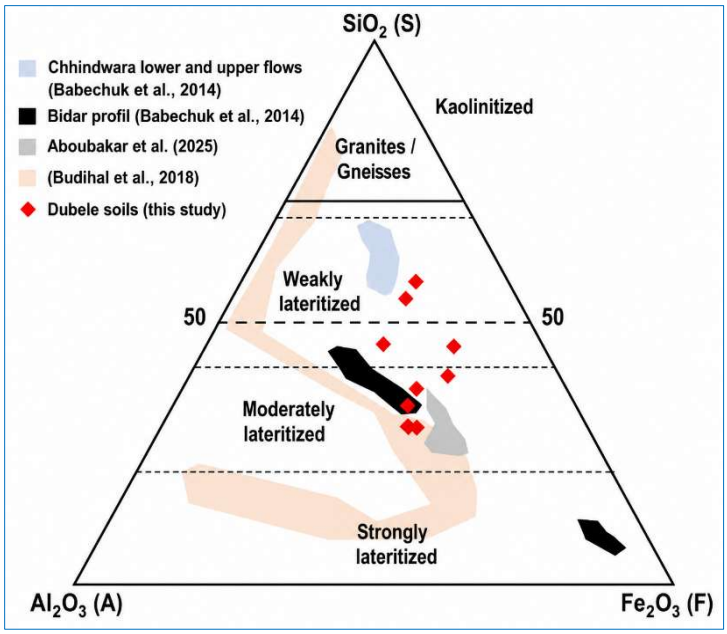

Fig. 9. Position of the Dubele lateritic soils in the SiO_2–Al_2O_3–Fe_2O_3 ternary diagram (after Schellmann, 1986)

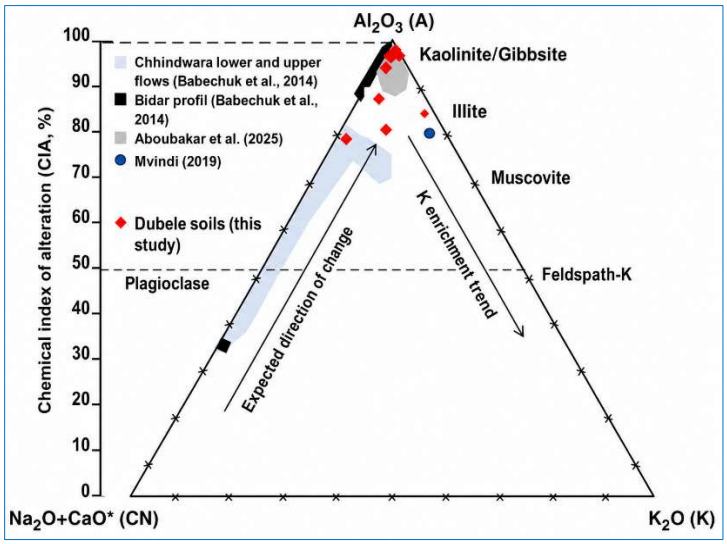

Fig. 10. Position of the Dubele lateritic soils in the Al_2O_3–CaO^*+Na_2O–K_2O (A–CN–K) molar diagram (after Nesbitt et Young, 1982)

The AF–CNK–M diagram (Fig. 11; Babechuk et al., 2014) adds Mg to this picture. All Dubele samples cluster near the AF apex, confirming that feldspar dissolution and ferromagnesian breakdown proceeded proportionally, with Mg loss tracking the alkali and alkaline earth elements consistent with the high CIA, PIA, and MIA(O) values already reported. Ngaoundal laterites (Aboubakar et al., 2026) and southern Cameroon laterites (Onana et al., 2017) again plots almost identically to the other Dubele samples (Fig.11).

Bidar laterite profile (Babechuk et al., 2014) sits lower, reflecting deeper mobile element depletion before full AF enrichment. The eastern gravel laterites (Nzabakurikiza et al., 2012) and Obala laterites profiles in Central Cameroon (Mvindi, 2019) retained comparatively higher Mg, indicating

less advanced ferromagnesian alteration. Across all five diagrams (Figs. 7-11) the Dubele lateritic soils occupy a consistent and reproducible geochemical position: more evolved than the Chhindwara basaltic profiles (Babechuk et al., 2014), closely comparable to the Ngaoundal and southern Cameroon laterites (Aboubakar et al., 2025; Onana et al., 2017), and less mature than the Bidar profiles (Babechuk et al., 2014). Ca, Na, and Mg have been almost completely removed, K enrichment is minor and localized, and Al and Fe have accumulated residually, without the complete desilicification that would mark a mature ferricrete or bauxite.

This intermediate signature reflects a particular combination of mafic parent-rock composition (Archean greenstone lithologies), weathering duration under a humid tropical climate (Fig. 2), drainage regime, and geomorphological plateau stability (Fig. 1d), which governs the balance between kaolinitization and ferruginization at Dubele. The mineral assemblage inferred throughout kaolinite, goethite, hematite, and possibly gibbsite, offers the most internally consistent explanation for these trends, pending direct mineralogical confirmation by XRD.

The apparently contrasting indications provided by the weathering and lateritization indices are not contradictory because they record different aspects of regolith evolution. High CIA and PIA values primarily indicate extensive chemical alteration of primary silicates and strong depletion of mobile cations, particularly Ca, Na, and K. In contrast, the IOL, S/R, and related lateritization parameters more specifically reflect the relative redistribution of Si, Al, and Fe and the progression of desilicification and ferruginization. Therefore, the Dubele soils may have experienced intense chemical weathering without reaching an advanced degree of lateritic maturity. The combination of high CIA–PIA values with moderate lateritization indices thus suggests advanced chemical leaching but only moderate development of the ferruginous characteristics recorded in the sampled B-horizon.

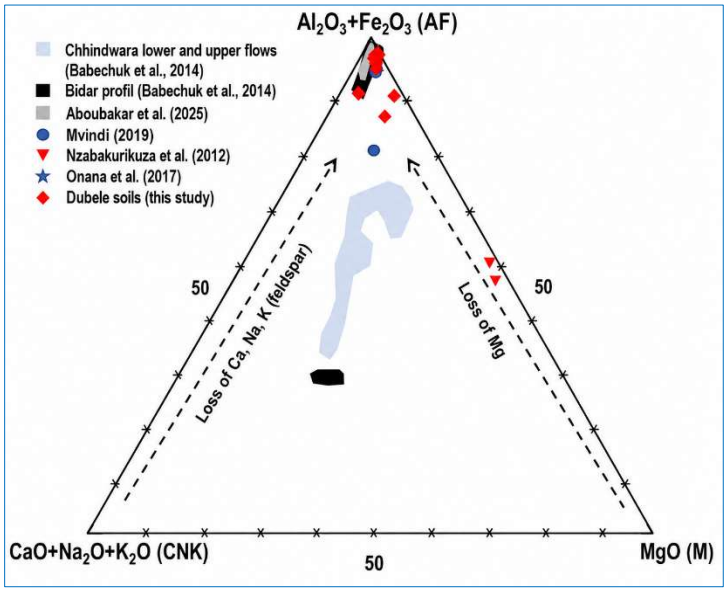

Fig. 11. Position of the Dubele lateritic soils in the AF–CNK–M diagram (Babechuk et al., 2014)

5.6. Trace-element Associations and Host Phases

The Pearson correlation matrix (Table 4) highlights a coherent trace element association in the Dubele lateritic soils, dominated by Ni, Cu, Zn, and As. Ni is strongly correlated with Cu ($r = 0.98$, $p < 0.001$), Zn ($r = 0.93$, $p < 0.001$), and As ($r = 0.87$, $p < 0.001$), while Cu shows similarly strong relationships with Zn ($r = 0.92$, $p < 0.001$) and As ($r = 0.92$, $p < 0.001$). The Zn–As correlation was also significant ($r = 0.79$, $p < 0.01$).

Together, these relationships indicate a closely coupled geochemical behavior during weathering. In gold-bearing greenstone terrains, Ni and Cu may reflect inheritance from mafic lithologies and sulfide-bearing assemblages, whereas As can be associated with arsenopyrite, pyrite, and other hydrothermal sulfides (Fridovsky et al., 2023; Huang et al., 2017; Groves et al., 1998). Within the Moto Greenstone Belt, the Ni–Cu–Zn–As association is consistent with a possible contribution from mineralized parent materials, followed by supergene redistribution (Mpaka et al., 2024).

Comparable preservation and redistribution of geochemical anomalies have been documented in weathering profiles over mineralized terrains (Freyssinet et al., 2005; Angélica et al., 1996). However, these correlations do not indicate a specific sulfide source or mineral host.

The presence of Co and V further strengthens this transition-metal association. Co correlated significantly with Zn ($r = 0.94$, $p < 0.01$), V ($r = 0.89$, $p < 0.01$), Cu ($r = 0.87$, $p < 0.05$), and Ni ($r = 0.85$, $p < 0.05$), although these relationships should be interpreted with caution because Co data were unavailable for three samples.

Vanadium was significantly associated with Zn ($r = 0.87$, $p < 0.01$), Ni ($r = 0.81$, $p < 0.01$), and Cu ($r = 0.75$, $p < 0.05$).

This V–Co–Ni–Cu–Zn assemblage may partly preserve the geochemical signature of the inferred mafic parent material, which is subsequently modified by tropical weathering and residual concentration (Freyssinet et al., 2005; Tardy, 1997; Schellmann, 1986).

Another important feature is the behavior of TiO_2 and P_2O_5. These oxides were strongly correlated ($r = 0.89$, $p < 0.001$). TiO_2 also correlates significantly with Zn, Ni, As, Cu, and V ($r = 0.67$–0.78), whereas P_2O_5 correlates with Zn, As, Cu, Ni, and V ($r = 0.74$–0.86). These relationships are compatible with coupled residual enrichment, as mobile constituents were progressively removed during intense weathering. The relative immobility of Ti favors its residual concentration in lateritic materials (Babechuk et al., 2014; Schellmann, 1986).

Resistant Ti-bearing phases, such as rutile, anatase, or ilmenite, as well as phosphate-bearing minerals, could therefore contribute to these patterns, but their presence cannot be confirmed without direct mineralogical analyses. Similarly, the significant As–TiO_2 ($r = 0.74$, $p < 0.05$) and As–P_2O_5 ($r = 0.82$, $p < 0.01$) relationships demonstrate covariation rather than common mineral hosts (Nesbitt and Young, 1982; Tardy, 1997).

Table 4. Correlation matrix of the Dubele soils

	TiO_2	Al_2O_3	Fe_2O_3	P_2O_5	SO_3	LOI	V	Cr	Co	Ni	Cu	Zn	As
TiO_2	1.00												
Al_2O_3	0.30	1.00											
Fe_2O_3	0.43	-0.03	1.00										
P_2O_5	0.89***	0.24	0.42	1.00									
SO_3	-0.19	-0.68*	-0.15	-0.09	1.00								
LOI	-0.61	-0.80**	-0.50	-0.63	0.63*	1.00							
V	0.67*	0.50	0.52	0.74*	-0.22	-0.82**	1.00						
Cr	0.56	-0.05	0.68*	0.60	0.08	-0.41	0.60	1.00					
Co	0.46	0.53	0.27	0.65	-0.34	-0.67	0.89**	-0.67	1.00				
Ni	0.77**	0.73*	0.23	0.79**	-0.50	-0.89***	0.81**	0.38	0.85*	1.00			
Cu	0.72*	0.68*	0.15	0.80**	-0.46	-0.83**	0.75*	0.37	0.87*	0.98***	1.00		
Zn	0.78**	0.54	0.24	0.86**	-0.18	-0.77**	0.87**	0.42	0.94**	0.93***	0.92***	1.00	
As	0.74*	0.46	0.18	0.82**	-0.37	-0.68*	0.62	0.57	0.68	0.87***	0.92***	0.79**	1.00

**: $p < 0.05$ → statistically significant correlation. **: $p < 0.01$ → very statistically significant correlation. ***: $p < 0.001$ → highly statistically significant correlation. No asterisk: $p \geq 0.05$ → statistically non-significant correlation*

In contrast, As was only weakly correlated with Fe_2O_3 ($r = 0.18$), and this relationship was not statistically significant. Therefore, variations in bulk Fe_2O_3 do not explain the As distribution among the analyzed samples. This does not exclude possible As retention by specific Fe-bearing secondary phases; however, such a mechanism cannot be demonstrated from bulk ED-XRF data alone.

Finally, LOI is negatively correlated with Ni ($r = -0.89$, $p < 0.001$), Cu ($r = -0.83$, $p < 0.01$), V ($r = -0.82$, $p < 0.01$), Zn ($r = -0.77$, $p < 0.01$), and As ($r = -0.68$, $p < 0.05$). This pattern is consistent with preferential trace element enrichment in the more residually concentrated components of the weathering material.

Overall, the correlation structure records the combined effects of parent rock inheritance, possible mineralization-related inputs, differential element mobility, residual enrichment, and supergene redistribution during tropical weathering (Babechuk et al., 2014; Freyssinet et al., 2005; Tardy, 1997; Schellmann, 1986). The proposed mineral hosts should nevertheless remain explicitly described as inferred until they can be tested using XRD, SEM–EDS, or mineral-scale chemical analyses.

6. Conclusion

This study provides a geochemical characterization of B-horizon lateritic soils from the Dubele area within the Neoarchean Moto Greenstone Belt in northeastern DR Congo. The major element composition and combined weathering indices (CIA, PIA, MIA, WIP, IOL, and S/R) indicate intense chemical weathering accompanied by substantial depletion of mobile alkali and alkaline-earth elements. The contrast between MIA(O) and MIA(R) is consistent with the relative Fe retention during weathering. However, the moderate lateritization indicated by some geochemical indices shows that high chemical weathering intensity does not necessarily correspond to an equally advanced degree of lateritic maturity. Therefore, these parameters record complementary but distinct aspects of weathering evolution.

The Al_2O_3/TiO_2 ratios, major-element discrimination diagrams, and Cr–Ni–V geochemical characteristics collectively suggest a predominantly mafic affinity of the parent material, consistent with the regional geological framework of the Moto Greenstone Belt. The strong SiO_2–Al_2O_3 relationship ($R^2 = 0.81$), in contrast to the weak SiO_2–Fe_2O_3 relationship ($R^2 = 0.02$), indicates the differential behavior of these major components during weathering. These bulk geochemical relationships may reflect the redistribution and residual concentration of elements during alteration, but they do not permit the identification of the mineral phases responsible for these patterns.

The trace-element data reveal a coherent Ni–Cu–Zn–As association, supported by statistically significant correlations between Ni–Cu ($r = 0.98$, $p < 0.001$), Ni–Zn ($r = 0.93$, $p < 0.001$), Cu–Zn ($r = 0.92$, $p < 0.001$), Cu–As ($r = 0.92$, $p < 0.001$), Ni–As ($r = 0.87$, $p < 0.001$), and Zn–As ($r = 0.79$, $p < 0.01$). Together with As concentrations reaching 2973 ppm, these relationships indicate a marked geochemical association that may reflect a combination of parent material inheritance, residual concentration, and supergene

redistribution. Nevertheless, the present dataset does not establish the primary source or mineralogical host of As in this study area. In particular, the weak and statistically non-significant As–Fe_2O_3 correlation (r = 0.18) shows that the bulk Fe concentration does not covary systematically with As and should not be used to infer or exclude specific As-bearing phases from the bulk composition.

The results should be considered within the limitations of the sampling strategy. The dataset comprises ten samples collected from the B horizon at approximately 0.5 m depth and therefore represents a surface B-horizon geochemical survey rather than complete vertical lateritic profiles. Consequently, the results characterize the sampled lateritic materials but cannot fully resolve the vertical geochemical variations within the weathered mantle.

Future investigations should extend sampling through complete weathering profiles and integrate X-ray diffraction (XRD), SEM–EDS, and mineral-scale chemical analyses. These approaches are required to identify mineral assemblages, determine the actual host phases of trace elements, and test the mineralogical interpretations suggested by the bulk geochemical data

Acknowledgements
The authors sincerely thank the technical staff of the Central Laboratory of Analyses at the Commissariat Général à l'Énergie Atomique/Centre Régional d'Études Nucléaires de Kinshasa (CGEA/CREN-K) for their invaluable assistance with the geochemical analyses conducted in this study. They are also grateful to the Faculty of Sciences of the University of Kisangani for granting official research authorization required for field investigations. Special thanks are given to the administrative, civil, and military authorities of the Dubele area for facilitating field activities and their cooperation throughout the sampling campaign. The authors further acknowledge the colleagues and reviewers whose constructive comments and valuable suggestions helped improve the scientific quality and clarity of this manuscript. This study did not receive any financial support from any funding agency. All fieldwork, laboratory analyses, and publication-related expenses were entirely covered by the authors. The authors declare no competing interests. Any remaining inaccuracies or omissions are the authors'sole responsibility.

Privacy Statement
The personal information provided during the manuscript submission process, including authors' names and email addresses, will be used exclusively for editorial management, peer review and publication purposes. This data will be handled confidentially and will not be disclosed to third parties or used for any purpose unrelated to the journal's editorial activities.

Data Availability
The data supporting the findings of this study are available from the corresponding author (Badriyo I.A.) upon reasonable request.

Conflict of interest
The authors declare that they have no competing interests. All authors approve the submission of this manuscript. The work is original, has not been published previously in whole or in part, and is not under consideration by any other journal.

Ethical approval
No experiments involving human participants or animals were carried out by the authors in the preparation of this work.

References
Abedini, A., Calagari, A.A., 2015. Erratum to: Mobilization and redistribution of major and trace elements in a lateritic profile: the Sheikh-Marut deposit, NW Iran. Arabian Journal of Geosciences 8 (12), 10883-10885. https://doi.org/10.1007/s12517-015-2010-5.

Aboubakar, A., Manefouet, I.B.K., Azefack, L.R.M., Tchedele, Y.L., Adoulko, D., Ntomb, D.Y., Mahamat, A., Wassouo, J.W., Fotze, Q.M.A., 2026. Morphological, mineralogical and geochemical characterization of Ngaoundal soils (Adamawa-Cameroon): Implications for weathering mechanisms and trajectories in tropical zones. Geosystems and Geoenvironment 5 (1), 100450. https://doi.org/10.1016/j.geogeo.2025.100450.

Amaya, A., Bertrant, B.S., Eric, B.E., Rexon, A.N., William, B.A., Bertrand, N.N., 2025. Provenance, weathering, and metallogenic characteristics of lateritic soils in the Koubou district, Eastern Cameroon. Arabian Journal of Geosciences 18, 85. https://doi.org/10.1007/s12517-025-12231-3.

Adeola, A.J., Dada, R.G., 2017. Mineralogical and geochemical trends in lateritic weathering profiles on basement rocks in Awa-Oru Ijebu and its environ, southwestern Nigeria. Global Journal of Geological Sciences 15 (1), 1-12. https://doi.org/10.4314/gjgs.v15i1.1.

Aleva, G.J.J., 1994. Laterites: Concepts, Geology, Morphology and Chemistry. In: International Soil Reference and Information Center (ISRIC), Ed., The Corlat Handbook, Corlat Technical Publication, Brussels, 8-21.

Andrew, A., Vargas, C., Mwandale, E., Kwibisa, J., Jongens, R., Quick, S., Komarnisky, N., Fanning, M., Bird, P., MacKenzie, D., Turnbull, R., Holliday, J., 2020. Orogenic Gold Deposits of the Kibali District, Neoarchean Moto Belt, Northeastern Democratic Republic of Congo. In Geology of the World's Major Gold Deposits and Provinces. Society of Economic Geologists. https://doi.org/10.5382/sp.23.09.

Angélica, R.S., da Costa, M.L., Pöllmann, H., 1996. Gold, wolframite, tourmaline-bearing lateritized gossans in the Amazon Region, Brazil. Journal of Geochemical Exploration 57 (1-3), 201-215. https://doi.org/10.1016/s0375-6742(96)00037-4.

Babechuk, M.G., Widdowson, M., Kamber, B.S., 2014. Quantifying chemical weathering intensity and trace element release from two contrasting basalt profiles, Deccan Traps, India. Chemical Geology 363, 56-75. https://doi.org/10.1016/j.chemgeo.2013.10.027.

Beauvais, A., 1999. Geochemical balance of lateritization processes

and climatic signatures in weathering profiles overlain by ferricretes in Central Africa. Geochimica et Cosmochimica Acta 63 (23-24), 3939-57. https://doi.org/10.1016/s0016-7037(99)00173-8.

Beck, H.E., Zimmermann, N.E., McVicar, T.R., Vergopolan, N., Berg, A., Wood, F.F., 2018. Present and future Köppen-Geiger climate classification maps at 1-km resolution. Scientific Data 5, 180214. https://doi.org/10.1038/sdata.2018.214.

Birimwiragi Namogo, D., Akame, J.M., Mbuluyo, M., Debaille, V., Itulamya, A.L.M., Hubert-Ferrari, A., 2025. Geology of the Isiro-Ngayu gold-bearing region, western belts of the Kibali granite-greenstone superterrane in the northeastern Congolese craton, Democratic Republic of Congo, EGU General Assembly 2025, Vienna, Austria, 27 Apr–2 May 2025, EGU25-13796. https://doi.org/10.5194/egusphere-egu25-13796.

Bitom, D., Volkoff, B., Beauvais, A., Seyler, F., Ndjigui, P-D., 2004. Rôle des héritages latéritiques et du niveau des nappes dans l'évolution des modelés et des sols en zone intertropicale forestière humide. Comptes Rendus. Géoscience 336 (13), 1161-1170. https://doi.org/10.1016/j.crte.2004.03.019.

Braun, J-J., Kabongo, E.K., Audry, S., Franck, D., Damien, D., Pascal, M., Mathieu, N., Denis, T., 2026. Geology and Geodynamics Evolution of the Congo Basin. In Resilience and Sustainability in the Congo Basin. Springer Nature Switzerland. https://doi.org/10.1007/978-3-032-02023-9_2-1.

Budihal, R., Pujar, G., 2018. Major and trace elements geochemistry of laterites from the Swarnagadde Plateau, Uttar Kannada District, Karnataka, India. Journal of Geosciences and Geomatics 6 (1), 12-20. https://doi.org/10.12691/jgg-6-1-2.

Burke, K., Gunnell, Y., 2008. The African Erosion Surface: A Continental-Scale Synthesis of Geomorphology, Tectonics, and Environmental Change over the Past 180 Million Years. In Memoir 201: The African Erosion Surface: A Continental-Scale Synthesis of Geomorphology, Tectonics, and Environmental Change over the Past 180 Million Years. Geological Society of America. https://doi.org/10.1130/2008.1201.

Butt, C.R.M., Anand, R.R., 2025. The Role of Regolith Formation and Evolution in the Development of Supergene Mineral Deposits. In Geology, Geochemistry and Formation of Supergene Mineral Deposits in Deeply Weathered Terrain. Springer Nature Switzerland. https://doi.org/10.1007/978-3-031-75733-4_3.

Cahen, L., Snelling, N.J., Delhal, J., Vail, J.R., Bonhomme, M., Ledent, D., 1984. The geochronology and evolution of Africa. London: Oxford.

Driese, S.G., 2004. Pedogenic Translocation of Fe in Modern and Ancient Vertisols and Implications for Interpretations of the Hekpoort Paleosol (2.25 Ga). Journal of Geology 112 (5), 543-560. https://doi.org/10.1086/422665.

Duzgoren-Aydin, N.S., Aydin, A., Malpas, J., 2002. Re-assessment of chemical weathering indices: case study on pyroclastic rocks of Hong Kong. Engineering Geology 63 (1-2), 99-119. https://doi.org/10.1016/S0013-7952(01)00073-4.

Fedo, C.M., Young, G.M., Nesbitt, H.W., 1997. Paleoclimatic control on the composition of the Paleoproterozoic Serpent Formation, Huronian Supergroup, Canada: a greenhouse to icehouse transition. Precambrian Research 86 (3-4): 201-23. https://doi.org/10.1016/S0301-9268(97)00049-1.

Freyssinet, PH., Butt, C.R.M., Morris, R.C., Piantone, P., 2005. Ore-Forming Processes Related to Lateritic Weathering. In *One* Hundredth Anniversary Volume. Society of Economic Geologists. https://doi.org/10.5382/av100.21.

Fridovsky, V.Y., Polufuntikova, L.I., Kudrin, M.V., 2023. Origin of Disseminated Gold-Sulfide Mineralization from Proximal Alteration in Orogenic Gold Deposits in the Central Sector of the Yana–Kolyma Metallogenic Belt, NE Russia. Minerals 13 (3), 394. https://doi.org/10.3390/min13030394.

Ghosh, S., Guchhait, S.K., 2019. Geochemical Properties and Lateritization Processes. In Laterites of the Bengal Basin. Springer International Publishing. https://doi.org/10.1007/978-3-030-22937-5_6.

Goodwin, A.M., 1991. Evolution of the Continental Crust. In Precambrian Geology. Elsevier. https://doi.org/10.1016/b978-0-12-289870-9.50011-4.

Groves, D.I., Goldfarb, R.J., Gebre-Mariam, M., Hagemann, S.G., Robert, F., 1998. Orogenic gold deposits: A proposed classification in the context of their crustal distribution and relationship to other gold deposit types. Ore Geology Reviews 13 (1-5), 7-27. https://doi.org/10.1016/s0169-1368(97)00012-7.

Guillocheau, F., Simon, B., Baby, G., Bessin, P., Robin, C., Dauteuil, O., 2018. Planation surfaces as a record of mantle dynamics: The case example of Africa. Gondwana Research 53, 82-98. https://doi.org/10.1016/j.gr.2017.05.015.

Hampl, F.J., Schiperski, F., Schwerdhelm, C., Stroncik, N., Bryce, C., von Blanckenburg, F., Neumann, T., 2023. Feedbacks between the formation of secondary minerals and the infiltration of fluids into the regolith of granitic rocks in different climatic zones (Chilean Coastal Cordillera). Earth Surface Dynamics 11 (3), 511-28. https://doi.org/10.5194/esurf-11-511-2023.

Hannigan, R., Brookfield, M.E., 2013. Inorganic geochemistry of the type Caradoc series (Sandbian to middle Katian, Upper Ordovician), Onny valley, Shropshire, UK. Geological Magazine 150 (4), 699-727. https://doi.org/10.1017/s0016756812000830.

Hayashi, K-I., Fujisawa, H., Holland, H.D., Ohmoto, H., 1997. Geochemistry of ~1.9 Ga sedimentary rocks from northeastern Labrador, Canada. Geochimica et Cosmochimica Acta 61 (19), 4115-37. https://doi.org/10.1016/s0016-7037(97)00214-7.

He, F., Van Espen, P.J., 1991. General approach for quantitative energy dispersive x-ray fluorescence analysis based on fundamental parameters. Analytical Chemistry 63 (20), 2237-2244. https://doi.org/10.1021/ac00020a009.

Huang, Q., Kamenetsky, V.S., Ehrig, K., McPhie, J., Kamenetsky, M., Apukhtina, O., Chambefort, I., 2017. Effects of hydrothermal alteration on mafic lithologies at the Olympic Dam Cu-U-Au-Ag deposit. Precambrian Research 292, 305-322. https://doi.org/10.1016/j.precamres.2017.02.013.

Iglesias-Martínez, M., Espí, J.A., Salama, W., Anand, R.R., Butt, C.R.M., 2024. Exploration and mining of lateritic gold (Part II): Resource estimation, geometallurgy and environmental considerations. Ore Geology Reviews 172, 106207. https://doi.org/10.1016/j.oregeorev.2024.106207.

JCGM 100, 2008. Evaluation of Measurement Data—Guide to the Expression of Uncertainty in Measurement. http://www.bipm.org/utils/common/documents/jcgm/JCGM_100_2008_E.pdf.

Kabete, J.M., McNaughton, N.J., Bashizi, A., Kiza, B., 2021a. Geologic-tectonic setting of the gold-endowed Kilo Terrane in the eastern Central Kibalian Superterrane, northeastern Democratic Republic of Congo. Precambrian Research 359, 106182. https://doi.org/10.1016/j.precamres.2021.106182.

Kabete, J. M., McNaughton, N.J., Bashizi, A., Kiza, B., 2021b. U-Pb SHRIMP geochronology data from the eastern Central Kibalian Superterrane, Bomu-Kibalian Craton, northeastern DRC: Implications for the tectonic evolution of the Kilo Terrane. Data in Brief 37, 107213. https://doi.org/10.1016/j.dib.2021.107213.

Kaboré, Z.G., Ziyani, L., Nouali, M., Pedraza, A., Duc, M., 2026.

Comprehensive Characterization of Lateritic Gravels for Road Construction: Correlation Between Geotechnical, Chemical and Mineralogical Properties. In Proceedings of the RILEM Spring Convention and Conference 2025. Springer Nature Switzerland. https://doi.org/10.1007/978-3-032-14166-8_46.

Kadima, E., Delvaux, D., Sebagenzi, S.N., Tack, L., Kabeya, S.M., 2011. Structure and geological history of the Congo Basin: an integrated interpretation of gravity, magnetic and reflection seismic data. Basin Research 23 (5), 499-527. https://doi.org/10.1111/j.1365-2117.2011.00500.x.

Long, G.L., Winefordner, J.D., 1983. Limit of Detection A Closer Look at the IUPAC Definition. Analytical Chemistry 55 (07), 712A-724A. https://doi.org/10.1021/ac00258a724.

McLennan, S.M., 1993. Weathering and global denudation ». The Journal of Geology 101 (2), 295-303. http://www.jstor.org/stable/30081153.

McLennan, S.M., Bock, B., Hemming, S.R., Hurowitz, J.A., Lev, S.M., McDaniel, D.K., 2003. The roles of provenance and sedimentary processes in the geochemistry of sedimentary rocks. In: Geochemistry of Sediments and Sedimentary Rocks: Evolutionary Considerations to Mineral Deposit-Forming Environments, Editor(s) D.R. Lentz, Geological Association of Canada. https://doi.org/10.12789/2003gts4/7.38.

Mpaka, Y.W., von der Heyden, B.P., Lawrence, D., Bampata, T., Ndongani, F.L., Mwandale, E., 2023. A paleoplacer component to the gold hosted in meta-conglomeratic units of the Neoarchaean moto greenstone belt, DRC. Ore Geology Reviews 157, 105477. https://doi.org/10.1016/j.oregeorev.2023.105477.

Mpaka, Y.W., von der Heyden, B.P., Glynn, S., Hurst, G., Lawrence, D., Bampata, T., Mwandale, E., 2024. Multistage evolution of gold mineralization in the Kibali gold district: Insights from pyrite analyses. Journal of African Earth Sciences 214, 105244. https://doi.org/10.1016/j.jafrearsci.2024.105244.

Mvindi, A.T.N., 2019. Caracterisation chimique, mineralogique et geotechnique des graveleux lateritiques d'obala-mbandjock (centre cameroun) en vue de leur utilisation en construction routiere ». PhD Thesis, Université de Yaoundé I., Cameroon.

Nahon, D.B., 1991. Self-organization in chemical lateritic weathering. Geoderma 51 (1-4), 5-13. https://doi.org/10.1016/0016-7061(91)90063-y.

Mvindi, N., Thierry, A., Atouba, L.C.O., Bineli, M.T.N., et al. 2024. Influence of mineralogical and geochemical multi-parameters on the geotechnical properties of gneiss-derived lateritic gravels from an equatorial zone, center Cameroon. Arabian Journal of Geosciences 17 (5), 165. https://doi.org/10.1007/s12517-024-11954-z.

Nesbitt, H.W., Young, G.M., 1982. Early Proterozoic climates and plate motions inferred from major element chemistry of lutites. Nature 299 (5885), 715-17. https://doi.org/10.1038/299715a0.

Nzabakurikiza, A., Onana, V.L., Likiby, B., Ndome Effoudou, P., Kamgang Kabeyene, P.V., Ekodeck, G.E., 2012. Chemical and mineralogical methods in the indentification of laterite gravels over migmatites for engineering purposes. Rev. CAMES-Série A 13: 28-33.

Okrusch, M., Frimmel, H.E., 2020. Weathering and Mineral Formation in Soils. In Mineralogy. Springer Berlin Heidelberg. https://doi.org/10.1007/978-3-662-57316-7_24.

Oyelami, C.A., van Rooy, J.L., 2016. A review of the use of lateritic soils in the construction/development of sustainable housing in Africa: A geological perspective. Journal of African Earth Sciences 119, 226-37. https://doi.org/10.1016/j.jafrearsci.2016.03.018.

Parker, A., 1970. An Index of Weathering for Silicate Rocks. Geological Magazine 107 (6), 501-504. https://doi.org/10.1017/s0016756800058581.

Peel, M.C., Finlayson, B.L., McMahon, T., 2007. Updated world map of the Köppen-Geiger climate classification. Hydrology and Earth System Sciences 11 (5), 1633-44. https://doi.org/10.5194/hess-11-1633-2007.

Price, J.R., Velbel, M.A., 2003. Chemical weathering indices applied to weathering profiles developed on heterogeneous felsic metamorphic parent rocks. Chemical Geology 202 (3-4), 397-416. https://doi.org/10.1016/j.chemgeo.2002.11.001.

Pszonicki, L., Hanna, A.N., Suschny, O., 1984. Report on intercomparison IAEA/Soil-6 of the determination of Cs-137, Pu-239, Ra-226, and Sr-90 in soil. International Atomic Energy Agency, Seibersdorf (Austria). Laboratories.

Roser, B.P., Korsch, J.R., 1988. Provenance signatures of sandstone-mudstone suites determined using discriminant function analysis of major-element data. Chemical Geology 67 (1-2), 119-39. https://doi.org/10.1016/0009-2541(88)90010-1.

Rossiter, DG., 2004. Digital soil resource inventories: status and prospects. Soil Use and Management 20 (3), 296-301. https://doi.org/10.1111/j.1475-2743.2004.tb00372.x.

Rousseau, R.M., 2006. Corrections for matrix effects in X-ray fluorescence analysis—A tutorial. Spectrochimica Acta Part B: Atomic Spectroscopy 61 (7), 759-77. https://doi.org/10.1016/j.sab.2006.06.014.

Schellmann, W., 1986. A new definition of laterite. Memoirs of the Geological Survey of India 120, 1-7.

Schwertmann, U., 1993. Relations Between Iron Oxides, Soil Color, and Soil Formation. In Soil Color. Wiley, janvier. https://doi.org/10.2136/sssaspecpub31.c4.

Schwertmann, U., Taylor, R.M., 1989. Iron Oxides. In Minerals in Soil Environments. Wiley, janvier. https://doi.org/10.2136/sssabookser1.2ed.c8.

Sivarajasingham, S., Alexander, L.T., Cady, J.G., Cline, M.G., 1962. Laterite. In Advances in Agronomy. Elsevier. https://doi.org/10.1016/s0065-2113(08)60435-6.

Tack, L., Wingate, M.T.D., De Waele, B., Belousova, E., Griffin, B., Tahon, A., Fernandez-Alonso, M., 2010. The 1375MaKibaran event" in Central Africa: Prominent emplacement of bimodal magmatism under extensional regime. Precambrian Research 180 (1-2), 63-84. https://doi.org/10.1016/j.precamres.2010.02.022.

Tardy, Y., 1997. Petrology of laterites and tropical soils. Geochemistry Department, University Louis Pasteur, Strasbourg, France.

Temgoua, É., Bitom, D., Bilong, P., Lucas, Y., Pfeifer, H-R., 2002. Démantèlement des paysages cuirassés anciens en zones forestières tropicales d'Afrique centrale : formation d'accumulations ferrugineuses actuelles en bas de versant. Comptes Rendus. Géoscience 334 (8), 537-43. https://doi.org/10.1016/s1631-0713(02)01793-5.

Turnbull, R.E., Allibone, A.H., Matheys, F., Fanning, C.M., Kasereka, E., Kabete, J., McNaughton, N.J., Mwandale, E., 2021. Geology and geochronology of the Archean plutonic rocks in the northeast Democratic Republic of Congo. Precambrian Research 358, 106133. https://doi.org/10.1016/j.precamres.2021.106133.

White, A.F., Brantley, S.L., 2003. The effect of time on the weathering of silicate minerals: why do weathering rates differ in the laboratory and field? Chemical Geology 202 (3-4), 479-506. https://doi.org/10.1016/j.chemgeo.2003.03.001.

Widdowson, M., 2007. Laterite and Ferricrete. In Geochemical Sediments and Landscapes. Wiley, janvier.

https://doi.org/10.1002/9780470712917.ch3.

Wit, M.J. de, Linol, B., 2014. Precambrian Basement of the Congo Basin and Its Flanking Terrains. In Geology and Resource Potential of the Congo Basin. Springer Berlin Heidelberg. https://doi.org/10.1007/978-3-642-29482-2_2.